

1 **Effect of scour on the fatigue life of offshore wind turbines and**
2 **its prevention through passive structural control**

3

4 Yu Cao¹, Ningyu Wu², Jigang Yang², Chao Chen^{1,3*}, Ronghua Zhu^{3,4*}, Xugang Hua¹,

5

6 ¹Key Laboratory for Bridge and Wind Engineering of Hunan Province, College of Civil
7 Engineering, Hunan University, Changsha, China

8 ²Hebei Construction Investment Offshore Wind Power Co., Ltd., Tangshan, China

9 ³Yangjiang Offshore Wind Laboratory, Yangjiang, China

10 ⁴Ocean College, Zhejiang University, Hangzhou, China

11

12

13

14

15

*Corresponding author: steinchen@hnu.edu.cn, zhu.richard@zju.edu.cn

16 **Abstract**

17 Offshore wind turbine (OWT) support structures are exposed to the risk of fatigue
18 damage and scour, and this risk can be effectively mitigated by installing structural
19 control devices such as tuned mass dampers (TMDs). However, time-varying scour al-
20 tering OWTs' dynamic characteristics has an impact on the TMD design and fatigue
21 life, which was rarely studied before. In this paper, a simplified modal model is used to
22 investigate the influence of scour and a TMD on the fatigue life evaluation of a 5 MW
23 OWT's support structure, and a traditional method and a newly developed optimization
24 technique are both presented to obtain TMD parameters. This optimization technique
25 aims at finding optimal parameters of the TMD which maximizes the fatigue life of a
26 hotspot at the mudline, and the effect of time-varying scour can be considered. This
27 study assumes that the TMD operates in the fore-aft (FA) direction, while the vibration
28 in the side-side (SS) direction is uncontrolled. Results show that scour can decrease the
29 fatigue life by about 24.1 %, and the TMD can effectively suppress vibration and in-
30 crease the fatigue life. When the scour depth reaches 1.3 times the pile diameter, the
31 TMD with a mass ratio of 1 % can increase the fatigue life of OWT's support structure
32 by about 64.6 %. Further, it is found that the fatigue life can be extended by 25 % with
33 the TMD optimized by the proposed optimization technique, compared to that with the
34 traditionally design method, which does not take the change of dynamic characteristics
35 into account.

36 **Keywords:** scour, offshore wind turbine, structural control, modal analysis, fatigue life.

37

38 **1 Introduction**

39 With the continuous development of large-size fixed-bottom OWTs, local scour
40 and scour protection of pile foundation have become a common issue (L. Wang et al.,
41 2020; X. Wang et al., 2019; F. Zhang et al., 2022). Scour has a significant impact on
42 the dynamic characteristics, vibration magnitudes, and thus fatigue life of OWTs under
43 wind and wave loads. On the one hand, the action of currents and waves causes local
44 scour pits around pile foundations, which reduces the burial depth of pile foundations.
45 This phenomenon usually causes a reduction in the natural frequencies of OWTs and
46 changes in other dynamic characteristics. This can potentially lead to resonance, large
47 amplitude stress cycles and fatigue damage when one of the natural frequencies is close

48 to the rotational frequency of the blades (Sørensen and Ibsen, 2013). On the other hand,
49 current scour protection measures cannot completely avoid scour and have their own
50 shortcomings. For example, armouring protection has the disadvantage that the projec-
51 tile cannot be accurately cast in complex sea conditions and is easy to be washed away
52 (G. Wang et al., 2023; F. Zhang et al., 2023). Flow-altering protection has the disad-
53 vantages of high cost and changing the dynamic characteristics of the foundation (Tang
54 et al., 2023). As offshore structures, wind turbines are vulnerable to corrosion from
55 seawater, which makes the fatigue problem worse (Amirafshari et al., 2021). Thus, the
56 scour-induced changes in dynamic characteristics and risk in resonance inevitably in-
57 duce a further increase in fatigue damage and deserve in depth research (Mayall et al.,
58 2018).

59 Many researchers have studied the effect of scour on fatigue damage accumulation
60 in OWTs. For instance, Tempel et al. (2006) investigated the frequency and fatigue of
61 piles under different scour depths and concluded that scour has a little effect on the
62 natural frequencies but a great effect on fatigue damage. Zhang et al. (2021) found that
63 scour depth has a significant influence on monopile impedance. Rezaei et al. (2018)
64 showed that scour leads to an increase in the maximum bending moment of the mono-
65 pile and a shortening of the fatigue life. To mitigate the fatigue damage in OWTs, in-
66 stallng structural control devices is an effective way. It was demonstrated that TMDs
67 have a positive effect on reducing vibration amplitudes of wind turbine systems (Lack-
68 ner and Rotea, 2011a; Dinh and Basu, 2015; Lu et al., 2023; Aydin et al., 2023). Dai et
69 al. (2021) conducted a shaker experiment using a scaled wind turbine model and
70 showed that the installed TMD can suppress the vibration of the structure more effec-
71 tively considering soil-structure interaction (SSI).

72 In the previously mentioned studies, researchers have individually investigated the
73 effect of scour on structural vibration and fatigue, and the structural control by TMDs
74 for OWTs. However, in practice, the effect of scour combining structural control via
75 TMDs could have a significant impact on OWTs' fatigue life. Moreover, whether con-
76 sidering scour could influence the design of TMDs, and TMDs with different parame-
77 ters can also have an impact on fatigue damage accumulation.

78 The purpose of this study is to explore the effect of scour on the fatigue life of
79 wind turbine structures and the control effect of TMD on the fatigue life of wind turbine
80 structures under scour conditions. The authors present a case study with a 5 MW single-

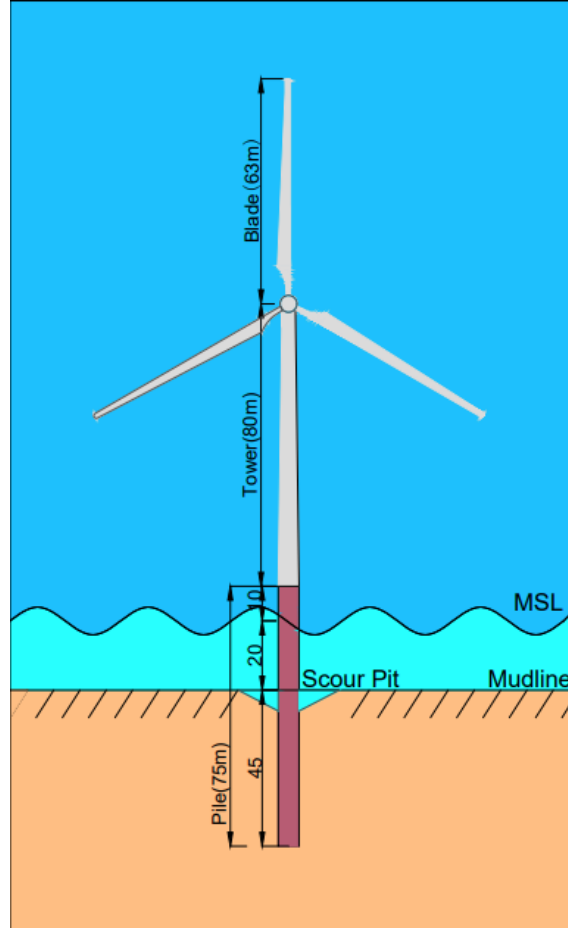
81 pile wind turbine to carry out related research. In this study, ABAQUS is used to estab-
82 lish a detailed SSI model with different scour depths. A finite element (FE) model con-
83 sidering wind loads and TMD is established in MATLAB, and the scour effect is con-
84 sidered by establishing a relationship with the ABAQUS model by means of the
85 equivalent stiffness matrix. And the finite element model is simplified to a modal model
86 for fast prediction of fatigue life. The TMD operates in the FA direction and does not
87 work in the SS direction. This study investigates the effect of different scour depths on
88 the performance of the TMD and the fatigue life of a 5 MW OWT's support structure
89 including a tower and a monopile foundation, and the optimization of the TMD's pa-
90 rameters considering time-varying scour depths to maximum fatigue life is also pre-
91 sented. This study provides some knowledge of the effects of the time varying scour
92 and the TMD on the fatigue life of wind turbines, as well as a new TMD design method
93 targeting at enhancing fatigue resistance. The rest of the paper is organized as follows:
94 Section 2 introduces the numerical models used in the research. Section 3 introduces
95 the traditional TMD design method and the newly developed parameter optimization
96 method. Section 4 describes the load cases for the fatigue analysis, the analysis results
97 of this study and the TMD parameter optimization results. Section 5 concludes the
98 study.

99 **2 Model description**

100 **2.1 Finite element model and implementation of tuned mass damper**

101 An FE model of a monopile-supported OWT installed with a TMD is established
102 in MATLAB. This model contains a flexible tower, a rotor-nacelle assembly (RNA),
103 and an external TMD, considering the foundation flexibility. The model is based on the
104 widely used NREL 5MW reference OWT, and its detailed properties are shown in Ta-
105 ble 1. Three-dimensional beam elements are used to create the FE model and the theo-
106 retical basis is the standard Euler-Bernoulli beam theory. The wind turbine tower is
107 divided into 18 beam elements, and the monopile between the mudline and the mean
108 sea level (MSL) are divided into 4 beam elements. A convergence test by comparing
109 the first natural frequencies shows that 22 beam elements are sufficient. Each element
110 node has 6 degrees of freedom (DOFs) corresponding to translational and rotational
111 motions in various directions. The mass matrix and stiffness matrix in the equation of
112 motion of the OWT structure can be obtained using the material properties. The damp-
113 ing matrix is applied by means of Rayleigh damping, and the combined damping ratio

114 of soil damping and structural damping is assumed to be 1 % (Chen and Duffour, 2018).
 115 The Rayleigh mass and stiffness coefficients α_1 and α_2 are defined by $\alpha_1 = \alpha_2 =$
 116 $\frac{\zeta_c}{\frac{1}{2\omega} + \frac{1}{2}}$. ω is the natural frequency of the first FA mode, and ζ_c is the combined damping
 117 ratio. The RNA is represented by a lumped mass at the tower top.



118

119 Fig. 1. Schematic of NREL 5MW wind turbine and scour effect

120 The TMD is mounted on the top of the tower, and the effect of the TMD is consid-
 121 ered by incorporating its mass, damping, and stiffness terms at relevant positions in the
 122 local mass, damping, and stiffness matrices of the beam element representing the top
 123 of the tower. The equation of motion of the OWT main structure is:

$$\begin{aligned} \mathbf{M}_s \ddot{\mathbf{U}}_s + \mathbf{C}_s \dot{\mathbf{U}}_s + \mathbf{K}_s \mathbf{U}_s + \mathbf{C}_T (\dot{\mathbf{U}}_s - \dot{\mathbf{U}}_T) + \mathbf{K}_T (\mathbf{U}_s - \mathbf{U}_T) \\ = \mathbf{F}_{\text{wind}} + \mathbf{F}_{\text{wave}}, \end{aligned} \quad (1)$$

124 where $\mathbf{M}_s, \mathbf{C}_s, \mathbf{K}_s$ are the mass, damping and stiffness matrices of the main structure.

125 $\mathbf{C}_T, \mathbf{K}_T$ are matrices with same dimensions containing c_T, k_T , $\mathbf{C}_T = \begin{bmatrix} 0 & \cdots & 0 \\ \vdots & \ddots & \vdots \\ 0 & \cdots & c_T \end{bmatrix}$, $\mathbf{K}_T =$

126 $\begin{bmatrix} 0 & \cdots & 0 \\ \vdots & \ddots & \vdots \\ 0 & \cdots & k_T \end{bmatrix}$. \mathbf{U}_s is the displacement vector of the main structure, $\mathbf{U}_s = \begin{bmatrix} u_{s-1} \\ \vdots \\ u_{s-top} \end{bmatrix}$.

127 \mathbf{U}_T is the displacement vector containing u_T , $\mathbf{U}_T = \begin{bmatrix} 0 \\ \vdots \\ u_T \end{bmatrix}$. $\mathbf{F}_{wind}, \mathbf{F}_{wave}$ are the aerody-

128 namic and wave load vectors. The equation of motion for the TMD can be represented

129 by

$$m_T \ddot{u}_T + c_T (\dot{u}_T - \dot{u}_{s-top}) + k_T (u_T - u_{s-top}) = 0, \quad (2)$$

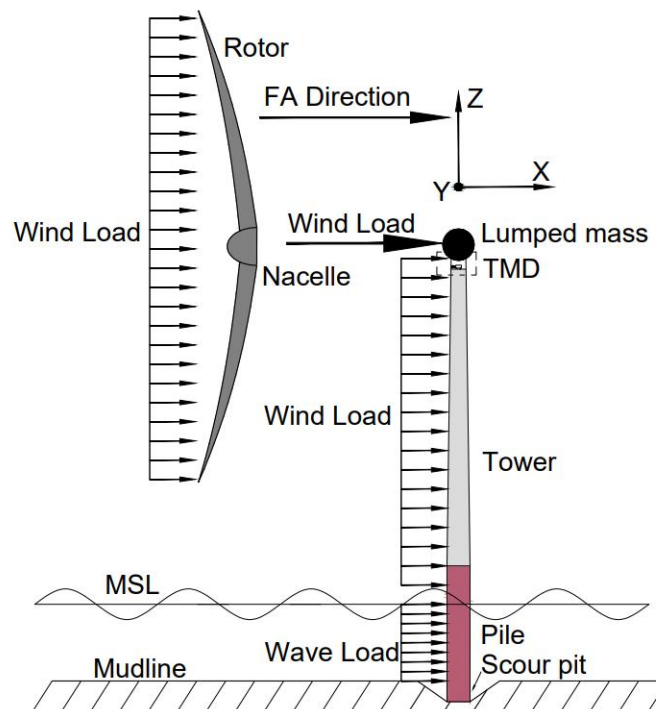
130 where m_T, c_T, k_T are the mass, damping and stiffness of the TMD, u_T, u_{s-top} are the
 131 displacement of the TMD and the displacement of the top node. The modelling of SSI
 132 is realized by an equivalent stiffness matrix, which will be introduced in detail subse-
 133 quently in Section 2.3.

134 Table 1. Basic properties of the NREL 5MW reference OWT (J. Jonkman et al., 2009;
 135 Rezaei, 2017)

Number of blade	3
Rotor diameter	126 m
Tower length	80 m
Tower diameter	3.87–6.00 m
Tower thickness	28–38 mm
Pile length	75 m
Pile penetration depth	45 m
Pile diameter	6 m
Pile thickness	80 mm
Hub height from MSL	92.4 m
Turbine mass	350000 kg
Blade mass	17740 kg
Rated wind speed	12.1 m/s

136 Wind loads were calculated using modified unsteady blade element momentum
 137 (BEM) theory (Branlard, 2017; B. J. Jonkman and Buhl, 2006) with Prandtl and Glauert
 138 corrections. Ignoring the iterative loop (Chen, Duffour, Fromme, et al., 2021) in the
 139 steady-state BEM code, the instantaneous aerodynamic forces were calculated for each

140 time step within the time integration. The turbulent wind field was generated using the
 141 Kaimal spectrum according to the wind field parameters of IEC 61400-3 (2019) as-
 142 suming moderate turbulence intensity. It should be noted that the aerodynamic loads
 143 from the rotor applied at the tower top were calculated using an aerodynamic force
 144 linearization technique previously developed by the authors (Chen, Duffour, Fromme,
 145 et al., 2021; Chen et al., 2020). This technique divides the aerodynamic loads into two
 146 parts. The first part is the quasi-steady aerodynamic force calculated by BEM theory,
 147 which does not consider the influence of tower top motion. The second part considers
 148 the effect of aerodynamic damping by introducing an additional aerodynamic damping
 149 matrix. The adoption of this technique aims to facilitate the development of a simplified
 150 modal model for rapid fatigue calculation, which will be introduced in detail in Sub-
 151 section 2.4. To represent the influence of controller in the OWT, a standard relationship
 152 (J. Jonkman et al., 2009) between the mean wind speed, rotor rotation speed, and blade
 153 pitch angles, which represents the OWT's normal operational conditions, are adopted
 154 throughout the wind loading calculations.



155

156

Fig. 2 Schematic of wind turbine load application

157

Wave loads were calculated using the Morison equation, which includes viscous
 158 drag and inertial forces:

$$\mathbf{F}_{\text{wave}} = \frac{1}{2} \rho_w D_{\text{pile}} C_d |\dot{\mathbf{u}}_w| \dot{\mathbf{u}}_w + \frac{\pi}{4} \rho_w D_{\text{pile}}^2 C_m \ddot{\mathbf{u}}_w, \quad (3)$$

159 where $\dot{\mathbf{u}}_w$ and $\ddot{\mathbf{u}}_w$ are the velocity and acceleration of water particles, C_d is the drag
 160 coefficient, D_{pile} is the diameter of the monopile between the mean sea level and the
 161 mudline, C_m is the inertia coefficient and ρ_w is the density of water. C_d and C_m were
 162 chosen as 1 and 2 respectively as the recommended values in Shirzadeh et al (2013).
 163 The wave profiles were obtained through the superposition of wave components, com-
 164 bining linear wave theory and JONSWAP spectra (Klaus et al., 1973). The application
 165 of wind and wave loads is shown in Fig. 2.

166 2.2 Scour modelling in ABAQUS

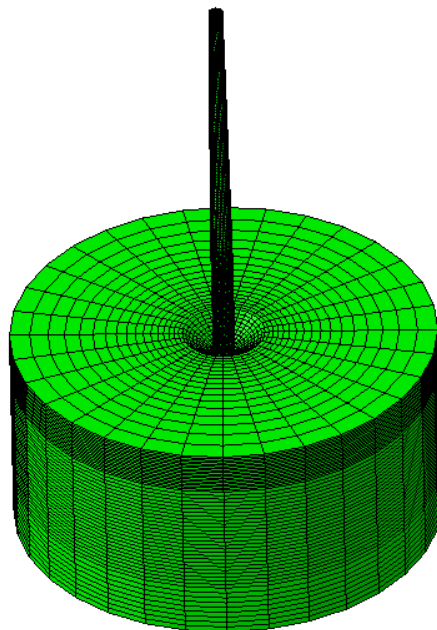
167 Using solid elements to model pile-soil interaction (S. Dai et al., 2021; Fard et al.,
 168 2022; Ma and Chen, 2021; Zdravković et al., 2015) is usually considered more accurate
 169 than the p-y curve method (Liang et al., 2018; Song and Achmus, 2023) and the equiv-
 170 alent embedding method (Shahmohammadi and Shabakhty, 2020; Bergua et al., 2022).
 171 The solid element method can also reduce the influence of empirical formula on the
 172 results. Therefore, the solid element method is used to establish the wind turbine scour
 173 model. The wind turbine scour model established in ABAQUS contains soil, pile foun-
 174 dation, tower, and the RNA is replaced by a concentrated mass located at the top of the
 175 tower. The diameter of the soil body is selected as 20 times the pile diameter, the soil
 176 under the pile foundation is selected as 2.5 times the pile diameter, and the total height
 177 of the soil body is 60 m. The soil body is made of homogeneous dense sandy soil, and
 178 the pile and tower are made of steel. The material parameters of the soil body, pile and
 179 tower are shown in Table 2 below:

180 Table 2. Soil, pile and tower material parameters

Type	Weight γ (kN/m ³)	modulus of elasticity E_s (MPa)	Poisson's ratio ν	Internal friction angle φ (°)	Expansion angle ψ (°)	Cohesion c (kPa)
Soil	19	80	0.3	35	23	0.1
Pile	78.5	215	0.25	-	-	-
Tower	85	215	0.25	-	-	-

181 The Mohr-Coulomb model is used for the soil, and the pile, tower, and nacelle are
 182 assumed to be elastic since they are much stiffer than the soil and do not deform

183 plastically under normal operational conditions. The pile and tower are connected by a
184 binding relationship. The normal contact between the pile and soil adopts the hard con-
185 tact, and the tangential contact adopts the friction penalty function. The relative sliding
186 friction factor at the interface, μ is equal to $\tan(0.75 \varphi)$, where φ is the internal friction
187 angle. The pile-soil contact is in the form of frictional contact, where mutual contact
188 pairs are established between the pile and the soil, including the contacts between the
189 pile bottom surface and the soil, the outside surface of the pile and the soil, and the
190 inside surface of the pile and the soil core. The frictional contact between pile bottom
191 surface and soil is omitted due to the small area of the contact surface. These frictional
192 contacts all adopt the face-to-face contact, and the contact discretization method adopts
193 the face-to-face discretization method, considering the large stiffness of the main sur-
194 face and the small stiffness of the slave surface. The perimeter of the soil body is trans-
195 lationally constrained, and the bottom surface of the soil adopts a fixed constraint. The
196 eight-node linear brick element (C3D8R) is used to model the pile and soil, and the
197 mesh division is realized by arranging seeds as shown in Fig. 3. The whole model is set
198 up by adopting the modelling method of “element birth and death”, which realizes the
199 operation of initial soil stress balance operation and sets up contacts and other related
200 steps by killing and activating relevant elements.



201

202

Fig. 3. Pile-soil interaction modelled by ABAQUS

203

204

The scour conditions can be represented by a deep conical pit around the pile under the long-term action of the waves and currents. According to the specification of Det

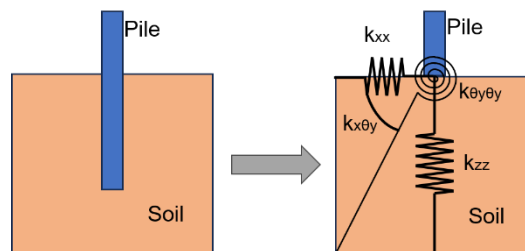
205 Norske Veritas (DNV) (2014b), the radius of the pit surface formed by scour, R, can
 206 be related to the depth of the scour pit by

$$R = \frac{D}{2} + \frac{S}{\tan\varphi}, \quad (4)$$

207 where D is the diameter of the pile, S is the scour depth, and φ is the angle of internal
 208 friction of the soil.

209 2.3 Equivalent stiffness matrix method

210 It is necessary to consider the effect of scour in the FE model in MATLAB. An
 211 equivalent stiffness matrix method is adopted in the FE model to consider the flexibility
 212 induced by SSI. The 6 DOFs of node at the mudline are assumed to be constrained by
 213 a series of coupled springs, and the stiffnesses of the coupled springs form a 6×6 stiff-
 214 ness matrix. For a specific stiffness term used in the FE model, for instance the one
 215 relevant to the lateral displacement in the FA direction, the value of the stiffness term
 216 can be found from the relationship between the reaction force at the mudline and the
 217 pile top displacement (Jung et al., 2015). The equivalent stiffness schematic of the pile-
 218 soil interaction in the FA direction for the OWT is shown in Fig. 4.



219

220 Fig. 4. Equivalent stiffness schematic of pile-soil interaction in the FA direction

221 According to the principle of virtual displacement and with the DOFs in other
 222 directions constrained, a unit displacement or rotation is first applied in one direction,
 223 and then the reaction force in that direction can be determined. The equivalent stiffness
 224 in that direction can be subsequently calculated by the relationship between the dis-
 225 placement and reaction force. Using the same approach, the stiffness terms correspond-
 226 ing to the remaining five DOFs are calculated. The stiffness terms in all the 6 DOFs
 227 together form all the diagonal terms of the soil stiffness matrix. With the diagonal terms
 228 known, the off-diagonal stiffness terms can be found by applying a unit displacement
 229 in one direction and looking at the reaction force in the other concerned direction, with

230 the other four DOFs constrained. Using the same principle, the off-diagonal terms can
 231 also be found from the relationship between the displacements and reaction forces,
 232 which ultimately results in a 6×6 stiffness matrix (Bergua et al., 2021; Pedersen and
 233 Askheim, 2021):

$$\mathbf{F}_{\text{soil}} = \begin{Bmatrix} F_x(t) \\ F_y(t) \\ F_z(t) \\ M_x(t) \\ M_y(t) \\ M_z(t) \end{Bmatrix} = \begin{bmatrix} k_{xx} & 0 & 0 & 0 & k_{x\theta y} & 0 \\ 0 & k_{yy} & 0 & k_{y\theta x} & 0 & 0 \\ 0 & 0 & k_{zz} & 0 & 0 & 0 \\ 0 & k_{\theta xy} & 0 & k_{\theta x\theta x} & 0 & 0 \\ k_{\theta yx} & 0 & 0 & 0 & k_{\theta y\theta y} & 0 \\ 0 & 0 & 0 & 0 & 0 & k_{\theta z\theta z} \end{bmatrix} \begin{Bmatrix} u_x(t) \\ u_y(t) \\ u_z(t) \\ \theta_x(t) \\ \theta_y(t) \\ \theta_z(t) \end{Bmatrix} \quad (5)$$

$$= \mathbf{K}_{\text{soil}} \mathbf{u}_{\text{soil}},$$

234 where \mathbf{K}_{soil} is the equivalent soil stiffness matrix, \mathbf{u}_{soil} is the displacement vector, and
 235 \mathbf{F}_{soil} is the reaction force vector. The equivalent soil stiffness matrix ignores the nonlin-
 236 earity in the force-displacement relationship. This approach is suitable for fatigue anal-
 237 ysis, as in normal operation conditions the deformation of the soil around the monopile
 238 is relatively small and the nonlinearity in soil stiffness is very weak. The 6×6 soil stiff-
 239 ness matrix obtained from ABAQUS is imported to the FE model in MATLAB. This
 240 modelling method combines the accuracy enhancement provided by the scour model in
 241 ABAQUS using solid elements with the fast calculation speed and convenience of ap-
 242 plying wind and wave loads using the FE model in MATLAB.

243 2.4 Rapid fatigue evaluation method

244 The established FE model in MATLAB can generate dynamic responses of the
 245 OWT, considering wind and wave loads and scour effect. However, a comprehensive
 246 fatigue life prediction in time domain needs to consider a large number of environmen-
 247 tal states and load cases, so simulation efficiency is very important. Moreover, the TMD
 248 design optimization requires much more dynamic response time series. The FE model
 249 is not fast enough in this case. Therefore, a simplified modal model is developed from
 250 the FE model in MATLAB following the method develop in Ref. (C .Chen et al., 2021).
 251 The total aerodynamic forces from the rotor applied on the tower top node are linearized
 252 as the sum of a term corresponding to the forces for an assumed rigid tower, and a term
 253 proportional to the tower top linear and angular velocities. The hydrodynamic forces
 254 are linearized by ignoring the relatively small monopile vibrations. The details for force
 255 linearization can be found in the authors' previous studies (Chen, Duffour, Fromme, et

256 al., 2021). Since the dynamic responses of the OWT are mainly dominated by the first
 257 two bending vibration modes, the FE model is reduced into a 4-DOF simplified modal
 258 model by considering only the first two bending modes in the FA and SS directions
 259 respectively. The development of the simplified 4-DOF modal model is briefly intro-
 260 duced as follows. Denoting the mass matrix and stiffness matrix of the OWT as \mathbf{M} and
 261 \mathbf{K} including the TMD and the lumped soil stiffness matrix, the undamped vibration
 262 mode matrix Ψ can be obtained directly through eigen analysis. According to the rela-
 263 tionship $\mathbf{u} = \Psi\alpha$ and multiplying the transpose of the undamped vibration matrix Ψ^T
 264 with the equation of motion, the following equation is obtained:

$$\Psi^T \mathbf{M} \Psi \ddot{\alpha} + \Psi^T \mathbf{C} \Psi \dot{\alpha} + \Psi^T \mathbf{K} \Psi \alpha = \Psi^T \mathbf{F}. \quad (6)$$

265 Then rewrite the above equation as

$$\bar{\mathbf{M}} \ddot{\alpha} + \bar{\mathbf{C}} \dot{\alpha} + \bar{\mathbf{K}} \alpha = \bar{\mathbf{F}}, \quad (7)$$

266 where α is the general coordinate vector, $\bar{\mathbf{M}}$ is the modal mass matrix, $\bar{\mathbf{C}}$ is the modal
 267 damping matrix, $\bar{\mathbf{K}}$ is the modal stiffness matrix, $\bar{\mathbf{F}}$ the modal load vector. Truncating
 268 Eq. (6) by only considering the first two bending modes, the FE model is reduced to a
 269 4-DOF modal model, which can be used for a rapid fatigue analysis. The dynamic re-
 270 sponses of the OWT can be obtained by modal superposition after solving the general
 271 coordinate vector by time integration. In the 4-DOF simplified modal model, the cross-
 272 section stress at any height can be calculated from the calculated node displacements.
 273 According to the dynamic stress extraction method provided by Pelayo et al. (Pelayo et
 274 al., 2015), the cross-section stress $\sigma_z(t)$ at any moment at a given location can be ob-
 275 tained by:

$$\sigma_z(t) = -E(\mathbf{N}^{e''}(z)\mathbf{u}_x^e(t)x + \mathbf{N}^{e''}(z)\mathbf{u}_y^e(t)y), \quad (8)$$

276 where \mathbf{u}^e is the nodal displacement vector at the cross section, E is the material elastic
 277 modulus, and \mathbf{N}^e is the elemental shape function vector of FE model, x and y are the
 278 positions within the section at the height z of the tower. After cyclic counting the stress
 279 time series using the rainfall counting method, the fatigue damage at the hotspot can be
 280 evaluated by utilizing the Palmgren-Miner rule based on the S-N fatigue calculation
 281 method. The S-N curve for steel under water can be obtained by the following equation
 282 considering the thickness effect in DNV (2014a):

$$\log N = \log \bar{a} - m \cdot \log \left[\Delta \sigma \left(\frac{t}{t_{\text{ref}}} \right)^k \right], \quad (9)$$

283 where N is the number of cycles to failure, $\Delta \sigma$ is the stress range. $\Delta \sigma$ is calculated from
 284 the nominal stress $\Delta \sigma_{\text{nominal}}$ by the equation $\Delta \sigma = \text{SCF} \cdot \Delta \sigma_{\text{nominal}}$, SCF is the stress
 285 concentration factor. m is the negative inverse slope of the S-N curve, and $\log \bar{a}$ is the
 286 intercept between the $\log N$ axis and the S-N curve, t_{ref} is the reference thickness for
 287 welded joints, t is the thickness at which cracks may grow. And $t = t_{\text{ref}}$ is used for
 288 thickness less than t_{ref} . When t is larger than t_{ref} , t is the actual thickness of the pile. k
 289 is the thickness exponent of fatigue strength. For pile joints, $t_{\text{ref}} = 25\text{mm}$. According
 290 to the DNV code, a bilinear S-N curve is usually used for offshore structures subjected
 291 mainly to typical wind and wave loads, using the Class E structural detail S-N curve
 292 shown in Table 3.

293 Table 3 Class E structural detail S-N curves

$N \leq 10^6$		$N \geq 10^6$		k	t (mm)	SCF
m_1	$\log \bar{a}_1$	m_2	$\log \bar{a}_2$			
3.0	11.610	5.0	15.350	0.2	80	1.13

294 For stresses with variable amplitudes, the fatigue damage index is calculated using
 295 the Palmgren-Miner summation rule:

$$D_k = \sum_{i=1}^{N_c} \frac{n_i}{N_i}, \quad (10)$$

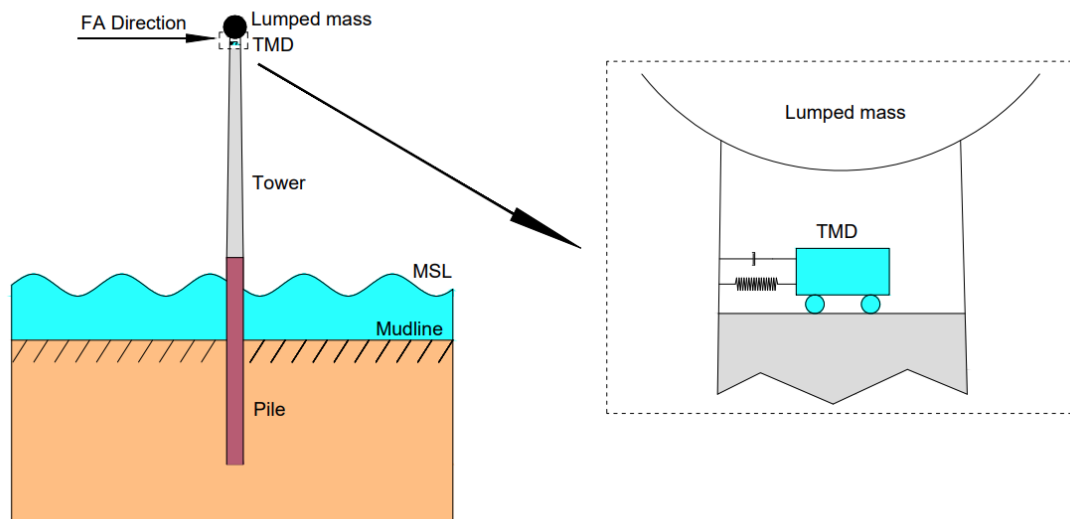
296 where N_c is the total number of bins, n_i is the number of cycles in i^{th} stress bin, N_i is
 297 the number of cycles to failure for the i^{th} stress range, and D_k is the total fatigue dam-
 298 age index. The ‘‘rainflow’’ function in MATLAB is used for rainflow counting. When
 299 a stress time history is provided, this function can automatically calculate the i^{th} stress
 300 range and the corresponding cycle number n_i , and N_c is the total number of stress
 301 ranges. Fatigue failure occurs at the hotspot when the fatigue damage index reaches
 302 unit 1.

303 3 Damper design and optimisation method

304 Installing damping devices can efficiently reduce the vibration amplitudes of
 305 OWTs so that their service life can be greatly prolonged. Using TMDs as passive

306 control devices is the most widely used method to control the vibration of OWT support
 307 structures. Usually, most TMDs are designed based on the dynamic characteristics of
 308 the OWTs determined in the preliminary design stage, without considering the changes
 309 in dynamic properties that may be caused by scour and soil degradation. In the real
 310 environment, scour can alter the dynamic characteristics of OWTs, potentially reducing
 311 the effectiveness of installed dampers or rendering them completely ineffective. There-
 312 fore, it is of great significance to consider the changes in dynamic properties caused by
 313 scour on the TMD design. The following two subsections first introduce the traditional
 314 TMD design method considering constant dynamic characteristics in the initial state.
 315 Then, an optimal parameter search method for the design of TMDs is presented, taking
 316 into account the effects of scour and fatigue life evaluation.

317 3.1 TMD design in initial state



318

319 Fig. 5. Schematic diagram of TMD arrangement in the tower tube

320 As the dominant vibration mode of the OWT structure in operation is the first
 321 bending mode, the largest vibration amplitude occurs at the top of the tower, making
 322 the installation of the TMD at the tower top most effective. Therefore, the TMD is
 323 installed inside the steel tube at the tower top to mainly control the vibration in the FA
 324 direction, as shown in Fig. 5. And the TMD can be aligned with the FA direction by
 325 rotating the damper. Accordingly, the initial design of the TMD is mainly carried out
 326 based on the dynamic properties for the first-order mode. The initial design is conducted
 327 based on the assumption that the monopile foundation is not scoured.

328 Numerous studies have shown that a TMD can effectively suppress the vibration
329 of a main structure when the mass ratio of the TMD to the main structure is 1 %-2 %
330 (Lackner and Rotea, 2011b; R. Zhang et al., 2019). After determining the mass ratio,
331 according to the classic TMD optimization theory proposed by Den Hartog (1957), the
332 optimal frequency ratio of the TMD to the OWT structure is

$$\alpha_{\text{opt}} = \frac{1}{1 + \mu}. \quad (11)$$

333 The optimal damping ratio for the TMD can be calculated by

$$\xi_{\text{opt}} = \sqrt{\frac{3\mu}{8(1 + \mu)}}, \quad (12)$$

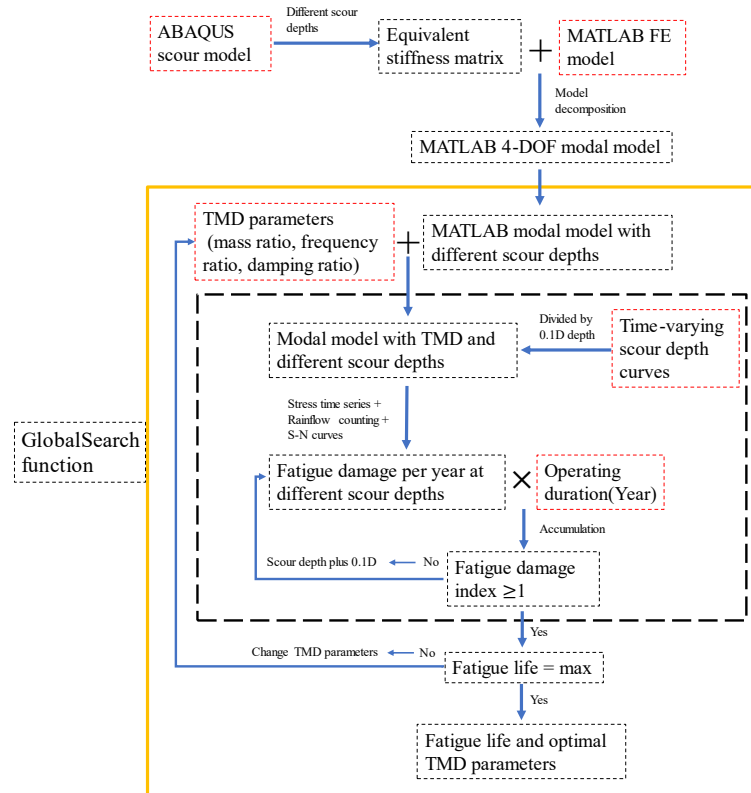
334 where μ is the mass ratio of the TMD to the OWT structure, α_{opt} is the optimal fre-
335 quency ratio of the TMD to the OWT structure and ξ_{opt} is the optimal damping ratio of
336 the TMD.

337 Considering that excessive mass will lead to increased construction costs, difficul-
338 ties, and changes in the inherent characteristics of the original structure, the mass ratio
339 of the TMD system to the main structure is initially set at 1 %. Moreover, previous
340 studies have found that a TLCD with a mass ratio of 1 % and a TMD with a mass ratio
341 of 2 % can effectively suppress vibration (Colwell and Basu, 2009; Lackner and Rotea,
342 2011b; R. Zhang et al., 2019). According to Den Hartog's optimization theory for the
343 initial TMD design, it can be determined that the optimal frequency ratio of the TMD
344 to the main structure is 0.99, and the optimal damping ratio of the TMD is 0.061. When
345 the OWT support structure is not scoured, the first-order modal mass of the structure is
346 440350 kg, and the first-order modal frequency is 0.265 Hz. Therefore, according to
347 the initial design parameters, the mass, stiffness coefficient and damping coefficient of
348 the TMD system are 4403.5 kg, 11,952 N/m and 885 N s/m respectively.

349 3.2 Fatigue-based damper optimisation technique

350 After scouring occurs around the monopile foundation, the burial depth of the
351 monopile and natural frequencies of the OWT gradually change. The vibration mitiga-
352 tion effect of the TMD designed based on the dynamic parameters in the initial state
353 can be reduced, which may lead to an increase in fatigue damage to the OWT support

354 structure. Therefore, when designing the TMD, considering the influence of time-var-
 355 ying scour can enhance the performance of the TMD and result in a longer fatigue life
 356 of the support structure.



357

358 Fig. 6. Flowchart of TMD fatigue-life-based optimization technique

359 Here a fatigue-life-based optimization technique (FOT) to find optimal parameters
 360 of the TMD is developed in MATLAB as shown in Fig. 6. In this technique, the fre-
 361 quency ratio, mass ratio and damping ratio of the TMD are set as the optimal parameters
 362 to be searched, with the optimization objective being the fatigue life. When considering
 363 the time-varying scour process, the time-varying scour depth curve is first divided into
 364 a number of scour depths with an increment of 0.1d. For each scour depth, the fatigue
 365 damage is calculated respectively and then the total fatigue damage in a particular du-
 366 ration can be summarised. When the scour pit becomes deeper, the fatigue damage ac-
 367 cumulates and finally reaches unit 1 which denotes the end of fatigue life. The simpli-
 368 fied 4-DOF modal model incorporating scour modelling is used to generate the stress
 369 time series. The optimization problem is formulated to determine the optimal parame-
 370 ters of the TMD that maximize the fatigue life of the OWT support structure. The
 371 “GlobalSearch” function in MATLAB is used to solve the optimization problem. In the
 372 TMD optimization process, the mass ratio of the TMD is initially set to 1 %, and only

373 the parameters of frequency ratio and damping ratio are optimized. Subsequently, in
 374 order to understand the optimization effect of TMD when the value of TMD mass ratio
 375 is not fixed, a mass ratio optimization interval is provided, making the mass ratio a
 376 variable within the optimization range.

377 4 Results

378 4.1 Environmental states and load cases

379 In this study, fatigue analyses are performed under 22 environmental states pro-
 380 vided by Tempel (2006), taking into account both operational and parked conditions.
 381 These 22 environmental states are shown in Table 4. In operating conditions, the wind
 382 turbine withstands the aerodynamic load of the rotating rotor and the wind load of the
 383 tower. The wind load on the rotor is calculated using the BEM theory. In parked con-
 384 ditions, the wind turbine mainly withstands the aerodynamic load on the tower, and the
 385 aerodynamic damping is very small. The aerodynamic loading on the blades is calcu-
 386 lated by directly looking at the aerodynamic loading coefficient table based on the local
 387 attack angles. The wind and wave loads are assumed to always act in the same direction
 388 to simplify the analysis. When the mean wind speeds are above the cut-in wind speed
 389 and below the cut-out wind speed, a 95 % wind turbine availability is assumed follow-
 390 ing the setting in Ref (Velarde et al., 2020), meaning that the OWT does not produce
 391 power for 5 % when the mean wind speeds are in the operating range. For a specific
 392 combination of mean wind speed, wave period, and wave height, six different random
 393 seed numbers are used to produce various wind fields and wave profiles, minimizing
 394 the impact of randomness. To obtain the stress time histories at the mudline, a 700 s
 395 simulation is conducted for each random seed, and the response in the first 100 s is
 396 subtracted to eliminate the effect of initial transient vibration. (Capaldo and Mella, 2023;
 397 Stieng and Muskulus, 2020).

398 Table 4. Environmental states, adopted from Tempel (van der Tempel, 2006).

State	Vw (m/s)	Tz (s)	Hs (m)	P _{State} (%)	State	Vw (m/s)	Tz (s)	Hs (m)	P _{State} (%)
1	4	3	0.5	3.95	12	14	5	2	3.26
2	4	4	0.5	3.21	13	16	4	2	1.79
3	6	3	0.5	11.17	14	16	5	2.5	3.1
4	6	4	0.5	7.22	15	18	5	2.5	1.74
5	8	3	0.5	11.45	16	18	5	3	0.8

6	8	4	1	8.68	17	20	5	2.5	0.43
7	10	3	0.5	5.31	18	20	5	3	1.14
8	10	4	1	11.33	19	22	5	3	0.4
9	12	4	1	5.86	20	22	6	4	0.29
10	12	4	1.5	6	21	24	5	3.5	0.15
11	14	4	1.5	4.48	22	24	6	4	0.1

399 In Table 4, V_w is the wind speed, T_z is the zero-crossing wave period, H_s is the
400 wave height, and P_{state} is the probability of environmental state. To investigate the ef-
401 fect of scour and installation of the TMD on the fatigue damage accumulation, six load
402 cases (LCs) are selected as shown in Table 5. LC 1 is used as the reference case, and
403 other cases are distinguished by different scour and TMD settings. For LC 4 to LC 6,
404 the initial design of the TMD with the mass ratio of 1 % is used.

405

Table 5. Load case definition

LC number	TMD condition	Scour condition	LC number	TMD condition	Scour condition
LC 1	No	No Scour	LC 4	Enable	No Scour
LC 2	No	Time-varying	LC 5	Enable	Time-varying
LC 3	No	Maximum	LC 6	Enable	Maximum

406 When considering the time-varying scour depth, for a particular time t , the time-
407 varying scour depth S can be predicted by the equation provided by Nakagawa et al.
408 (1976):

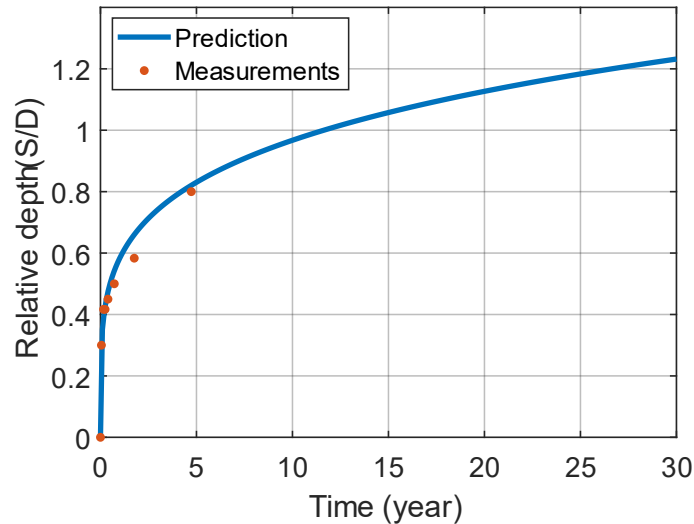
$$S = \left(\frac{t}{t_1}\right)^{0.22} D, \quad (13)$$

409 where D is the diameter of the monopile, t_1 is the reference time and can be calculated
410 by

$$t_1 = 29.2 \cdot \frac{D}{\sqrt{2} \cdot u} \cdot \left(\frac{\sqrt{\Delta \cdot g \cdot d_{50}}}{\sqrt{2} \cdot u - u_c}\right)^3 \cdot \left(\frac{D}{d_{50}}\right)^{1.9}. \quad (14)$$

411 u is the tidal velocity and taken as 0.5 m/s, u_c is the critical shear velocity and taken as
412 0.37 m/s, g is the acceleration of gravity and taken as 9.8 m/s², d_{50} is the grain size of
413 sea sand and taken as 0.2 mm. The parameter $\Delta = \frac{\rho_s}{\rho_w} - 1$, where ρ_s is the density of
414 sand and taken as 2.65 g/cm³, ρ_w is the density of water and taken as 1 g/cm³. Rudolph

415 et al. (Rudolph et al., 2016) provided information on the sea state and measured the
 416 scour depth in the North Sea where the monopile N7 is situated. The measured scour
 417 depth was fitted well for the first five years based on the time-varying scour depth pre-
 418 diction equation shown in Eq. (13). Therefore, the data from the North Sea site can
 419 represent a typical ocean environment with time-varying scour and is used for the cor-
 420 relation analysis in this study.



421

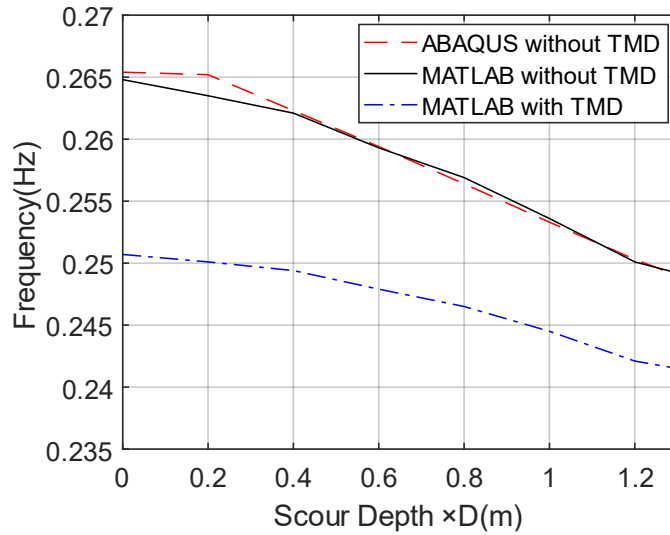
422 Fig. 7. Time-varying scour depth curve for pile N7 in the North Sea

423 When conducting an analysis with the time-varying scour, an increment of scour
 424 depth equal to $0.1D$ is utilized. At a specific scour depth, the fatigue damage is calcu-
 425 lated, and then the total fatigue damage during a longer period with varying scour
 426 depths can be obtained by damage accumulation. According to the specification of
 427 DNV, the maximum depth of a local scour pit formed around a pile foundation is 1.3
 428 times the diameter of the pile. Therefore, it is assumed that the local scour pit has a
 429 maximum scour depth of $1.3D$ at which the scour process achieves equilibrium.

430 4.2 Scour influence on natural frequencies

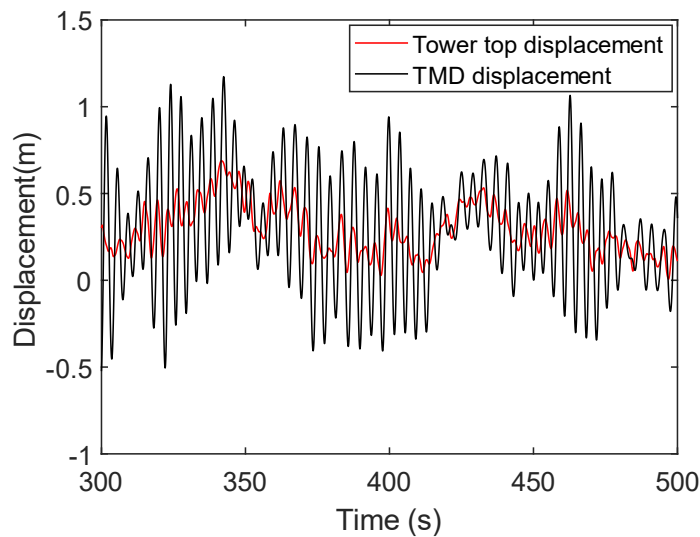
431 The scour of the soil around the monopile has an important effect on the natural
 432 frequencies of the OWT. For different scour depths, the first natural frequencies ob-
 433 tained the by the models in ABAQUS and MATLAB are compared in Fig. 8. It shows
 434 the increase in the scour depth leads to a decrease in the first natural frequency of the
 435 OWT. The first natural frequency is 0.265 Hz when no scour occurs, and the natural
 436 frequency is reduced to 0.248 Hz when the depth of the scour pit reaches the maximum
 437 depth. The first natural frequency is reduced by 6.42 % due to the maximum scour depth.

438 It shows that the natural frequency nearly monotonically decreases with the increase of
 439 the scour depth. The installation of TMD also influences the natural frequency of the
 440 OWT main structure. The TMD with a mass ratio of 1 % makes the first natural fre-
 441 quency of the OWT main structure reduce to 0.251 Hz when no scour occurs, meaning
 442 that the natural frequency is reduced by 5.28 %.



443

444 Fig. 8. Relationship between wind turbine natural frequency and scour depth



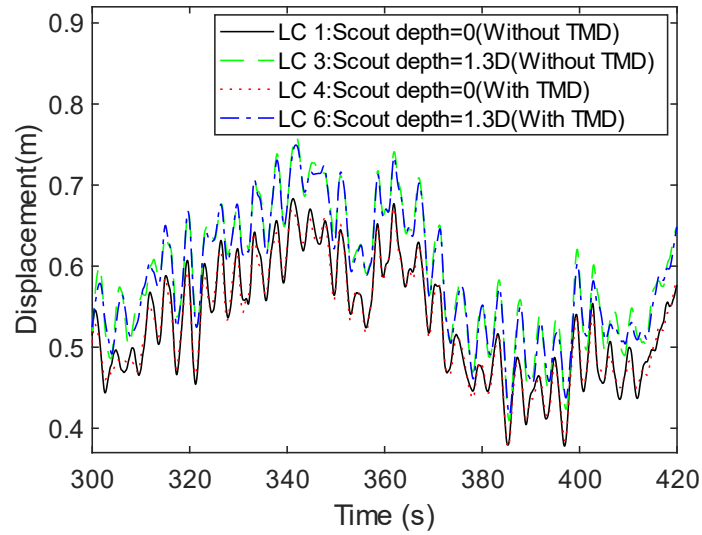
445

446 Fig. 9 Displacement of tower top and TMD under the 22nd environmental state

447 In the TMD design process, the feasible displacement should be considered. The
 448 smaller the mass ratio of TMD is, the larger the feasible displacement is required. The
 449 22nd environmental state corresponds to the greatest vibration responses of the wind
 450 turbine tower top due to large wind speed variations and lower aerodynamic damping,

451 and the stroke of the TMD can be the largest. As shown in Fig. 9, the relative displacement
452 between the TMD and the tower top is much less than the inner diameter of the
453 wind turbine tower top in the 22nd environmental state. It shows that the stroke of the
454 TMD is sufficient when the mass ratio of the TMD is 1 %.

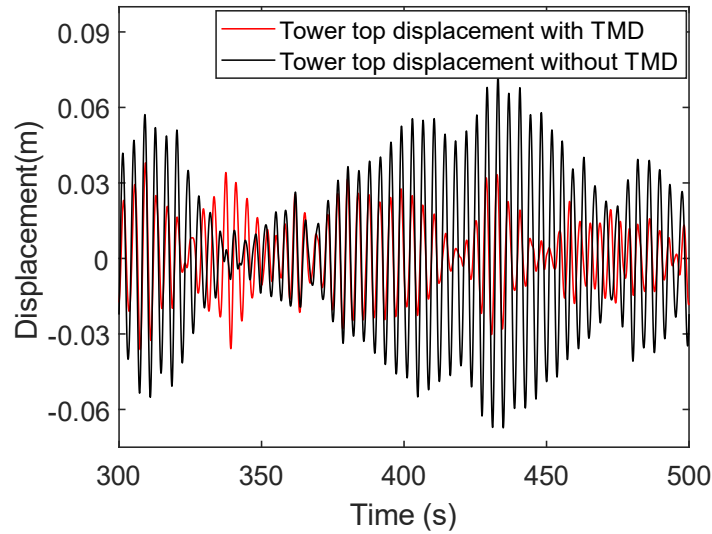
455 4.3 Dynamic response analysis



456

457 Fig. 10. Dynamic response of wind turbine under wind-wave coupled loads for four
458 operating conditions

459 When the OWT in the operating state is under the 9th environmental state which
460 corresponds to the rated wind speed of 12 m/s, a comparison for the tower top displacement
461 is made for LC 1, LC 3, LC 4 and LC 6, as shown in Fig. 10. These displacements
462 are obtained from the FE model in MATLAB described in Subsection 2.1. By comparing
463 the displacements from 300 seconds to 420 seconds for LC 1 and LC 4, it can be
464 found that the vibration amplitude of the tower top slightly decreases when the TMD is
465 installed. Moreover, by comparing the displacement responses for LC 1 and LC 3, it
466 can be found that the average of the displacement at the tower top increases when the
467 scour depth reaches 1.3D. This is because scour makes the OWT support structure become
468 more flexible. It is known that the aerodynamic damping is large when the OWT
469 is operating under the rated wind speed, so it is normal that the vibration mitigation
470 effect of the TMD is less significant in this case. The effect of the TMD is more prominent
471 for parked conditions with less aerodynamic damping. As shown in the Fig. 11,
472 the vibration mitigation effect of the TMD is more significant under the parked condition
473 with 3 m/s wind speed.

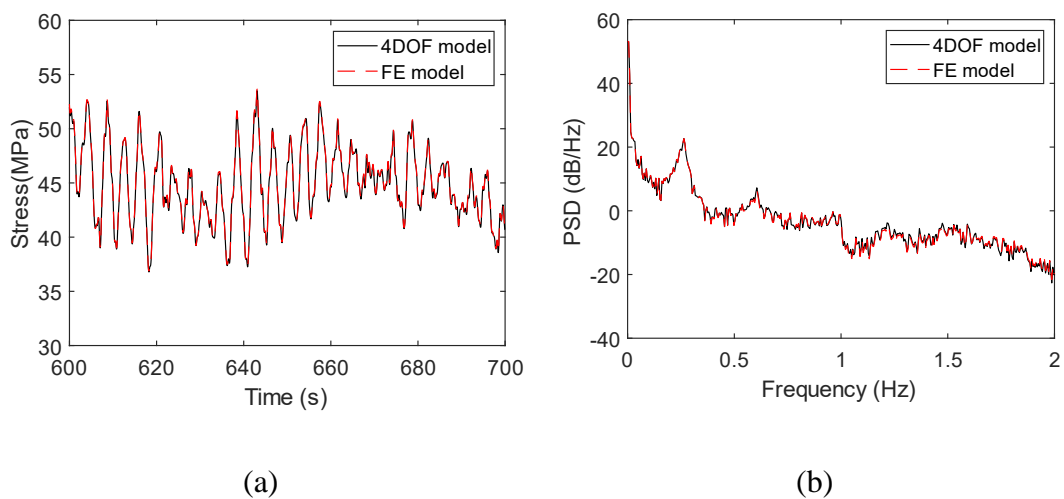


474

475 Fig. 11 The displacement response of wind turbine tower under the parked condition
 476 with 3 m/s wind speed

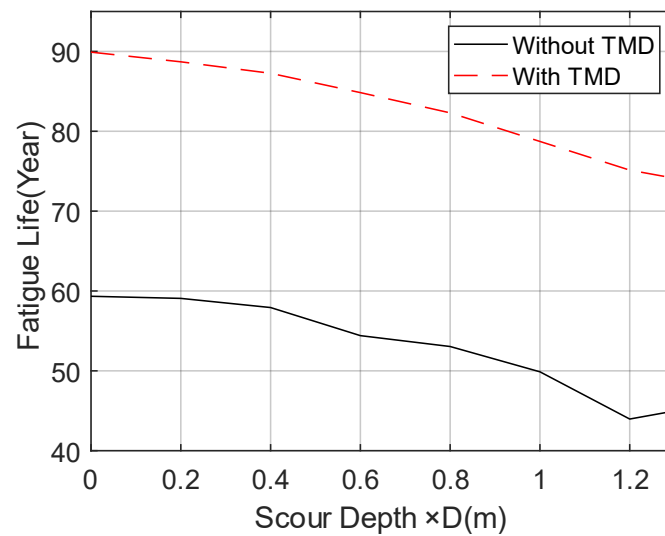
477 **4.4 Fatigue calculation results**

478 In Subsection 2.4, it is mentioned that in the process of fatigue life analysis, the 4-
 479 DOF simplified modal model is used to greatly save the calculation time. The accuracy
 480 test of the 4-DOF modal model in generating dynamic responses is first presented in
 481 this subsection. Under the turbulent wind field with a turbulence intensity of 11.9 %
 482 and an average wind speed of 12 m/s, the FE model and the 4-DOF simplified modal
 483 model are used to calculate the stress responses at the mudline for 10 minutes.



484 Fig. 12. Comparison of stresses at the mudline from the FE model and the 4-DOF
 485 model in time domain (a) and frequency domain (b)

486 As shown in Fig. 12, the stress responses from these two models are very close,
 487 confirming the accuracy of the 4-DOF modal model. The fatigue damage caused by the
 488 FE model in 10 min is 2.108×10^{-7} , and the fatigue damage caused by the 4-DOF
 489 model in 10 min is 2.1×10^{-7} , with an error of 0.05 %. Moreover, the calculation time
 490 of the 4-DOF simplified modal model is only about 1/55 of that of the FE model, which
 491 shows that the 4-DOF simplified modal model is adequate to replace the FE model
 492 when conducting fatigue life prediction.



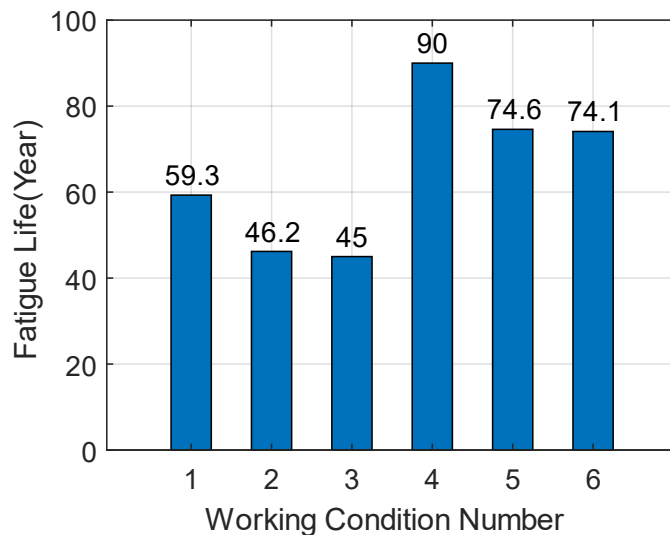
493

494 Fig. 13. Fatigue life of wind turbine with different scour depths

495 The 4-DOF simplified modal model is used to conduct fatigue life prediction for
 496 the OWT support structure under LC 1 to LC 6. A 10 min simulation is conducted for
 497 each of the six different random seed numbers to obtain stress time histories at the
 498 mudline. The location of the hotspot selected to assess fatigue damage is where the
 499 maximum stress occurs, specifically in the support structure cross-section at the mud-
 500 line. Although the location in the monopile where the moment reaches its maximum
 501 value can be below the mudline, the location at the mudline is chosen for simplicity.
 502 Further, since the SSI is modelled in the FE model by an equivalent soil stiffness matrix,
 503 it is not straightforward to determine the internal forces at the cross sections below the
 504 mudline. Given the stress time series at the selected hotspot, the corresponding fatigue
 505 damage is calculated. The fatigue damage for the combination of mean wind speed,
 506 wave period, and wave height over 10 minutes is calculated by averaging the fatigue
 507 damage across six random seeds. For all the 22 environment states, the 10 min fatigue
 508 damage are calculated. The fatigue life is predicted according to the Palmgren-Miner

509 sum rule by combining these calculated fatigue damage and the probabilities of the
510 environmental states.

511 For various scour depths, the fatigue life of the OWT considering both operating
512 and parked conditions is predicted with or without TMD installation, and the results are
513 shown in Fig. 13. It is shown that an increase in scour depth leads to a decrease in
514 fatigue life, and an increasing fatigue life reduction rate can be observed when the scour
515 depth increases. When no scour occurs and the TMD is not installed on the OWT, the
516 OWT's fatigue life is 59.3 years, and the fatigue life drops to 45.0 years when consid-
517 ering the maximum scour depth of 1.3 D. There exist some uncertainties in the fatigue
518 life prediction process due to the generation of random wind field and wave profile. It
519 should be noted that the predicted fatigue life is much longer than the normally adopted
520 OWTs' design fatigue life of 25-30 years. This can be explained by the following rea-
521 sons. First, the maximum moment of the OWT support structure is not at the cross-
522 section at the mudline where the selected hotspot is located. Second, the complex wind
523 and wave directionality during the OWT's lifetime is simplified, which can influence
524 the fatigue calculation results. Third, many other operational conditions such as start-
525 up and shut-down phases are not considered in this study, which can also impact fatigue
526 damage accumulation. Moreover, the installation of the TMD greatly extends about
527 51.8 % of the OWT support structure's fatigue life.



528

529 Fig. 14. Fatigue life of the wind turbine under six operating conditions

530 The fatigue life prediction results of the OWT are obtained for all the six LCs, as
531 shown in Fig. 14. The fatigue life of the reference case LC 1, which is 59.3 years, is

532 regarded as the reference fatigue life. It shows that the fatigue life decreases by 14.3
 533 years, or about 24.1 %, when the scour depth is set at the maximum value of 1.3D
 534 without applying the TMD, compared to the reference fatigue life. When considering
 535 the time-varying scour, the fatigue life decreases by about 22.1 % from the reference
 536 value. When comparing the results for LC 1 and LC 4, it shows the installation of the
 537 TMD results in a significant increase in the fatigue life of the OWT, with an increase
 538 in fatigue life of about 30.7 years, which is about 51.8 %. In LCs with the TMD installed,
 539 the fatigue life in LC 6 decreases by about 17.7 % when the scour depth reaches 1.3D,
 540 compared to the result in LC 4. But the fatigue life in LC 6 is still 1.25 times the refer-
 541 ence fatigue life, which indicates that the imposition of TMD can effectively increase
 542 the fatigue life of the OWT by reducing vibration amplitudes.

543 4.5 Fatigue calculation with optimized TMD

544 To compare the optimization effect and speed up the optimal parameter search
 545 process, the mass ratio of TMD is first kept as 1 %. Before the optimization, the param-
 546 eter ranges of the frequency ratio and damping ratio need to be defined. The optimal
 547 frequency of the TMD is usually close to the frequency of the main structure, so the
 548 range of the frequency ratio is chosen to be from 0.8 to 1.1 for optimization. As the
 549 optimal damping ratio can vary in a relatively larger range, the range of the damping
 550 ratio for optimization is chosen to be from 1 % to 30 %. The optimization of the TMD
 551 is also conducted with the mass ratio not fixed. A range of the mass ratio from 0.001 to
 552 0.1 is used to optimize the TMD so that the influence of the mass ratio can be evaluated.

553 Table 6. Optimization of TMD parameters

Optimization method	Mass ratio range	Time-varying scour	Optimal mass ratio	Optimal frequency ratio	Optimal damping ratio	Fatigue life (Year)
Initial (LC 5)	0.01	Use	0.01	0.99	0.061	74.6
FOT	0.01	Use	0.01	0.94	0.050	93.2
FOT	0.001-0.1	Use	0.097	0.92	0.150	133.2

554 The optimal parameters obtained by FOT, as well as the predicted fatigue life, are
 555 listed in Table 6. The fatigue life for LC 5 and the parameters of the initially designed
 556 TMD are also shown in Table 6 for comparison. It shows that when the mass ratio is
 557 fixed at 1 %, the optimal frequency ratio is 0.94, the optimal damping ratio is 5 %, and
 558 the final fatigue life is 93.2 years. Compared to the fatigue life with the initially

559 optimized TMD using the traditional method without considering scour, the fatigue life
560 increases by 18.6 years, which is approximately 25%. It indicates that the parameter
561 search in the optimization process is correct, and it is better to use the TMD parameter
562 search method to design the TMD after obtaining the time-varying scour curve. When
563 the mass ratio range is taken from 0.1 % to 10 %, the optimal mass ratio of the TMD is
564 9.7 %, the frequency ratio is 0.92, the damping ratio is 15 %, and the final fatigue life
565 is 133.2 years. In this case, the fatigue life of the OWT is significantly increased pri-
566 marily because of the large mass ratio. However, in practice, it may be uneconomical
567 to implement a TMD with such a large mass ratio.

568 5 Conclusions

569 This study establishes a rapid numerical model that can consider the effect of scour
570 and the installation of a TMD, and the TMD operates only in the FA direction. The
571 model is simplified by using concentrated mass instead of RNA and ignores the non-
572 linearity of the equivalent stiffness matrix. The established model is used to investigate
573 the influence of scour and the installed passive structural control device on the OWT's
574 natural frequencies and fatigue life through 22 environmental states. An optimization
575 technique has also been developed to find the optimal parameters of the TMD consid-
576 ering time-varying scour. Moreover, it shows that the vibration amplitude of the OWT
577 can be effectively reduced by the TMD. On the one hand, the results show that the TMD
578 reduces the vibration amplitude of the tower top. On the other hand, when the scour
579 depth reaches 1.3D, the wind turbine support structure becomes more flexible, with the
580 displacement of the tower top increasing without TMD.

581 In addition, the fatigue calculation results show that the installation of the TMD
582 significantly extends the fatigue life of the OWT, but scour can cause a reduced perfor-
583 mance of the TMD. It is found that when scour and the scour-induced natural frequency
584 reduction are considered during the OWT's lifetime, the performance of the initially
585 designed TMD is not as good as the TMD optimized by the developed FOT in terms of
586 fatigue life enhancement. Given a mass ratio of 1 %, the fatigue life can be extended by
587 25 % with the TMD optimized by FOT. This is because FOT can consider the effect of
588 time-varying scour. This study focuses solely on analysing scour, but it is important to
589 note that other factors like soil degradation can also impact the dynamic characteristics
590 of OWTs. These factors may influence on structural control devices and the evaluation
591 of fatigue life. Additionally, during OWTs' lifetime, the properties of installed TMDs

592 can also change, making the evaluation of TMDs' performance and OWTs' fatigue life
593 more complicated. These factors are worth investigating in the future.

594 **Author contribution**

595 Yu Cao: Investigation, Software, Validation, Formal Analysis, Writing - Original Draft

596 Ningyu Wu: Data Curation, Investigation

597 Jigang Yang: Validation, Software

598 Chao Chen: Conceptualization, Methodology, Writing - Review & Editing, Supervision,

599 Funding acquisition

600 Ronghua Zhu: Methodology, Resources

601 Xugang Hua: Writing - Review & Editing, Funding acquisition

602 **Competing interests**

603 The contact author has declared that none of the authors has any competing inter-
604 ests.

605 **Acknowledgements**

606 The financial supports from the National Natural Science Foundation of China (No.
607 52108280), Yangjiang Offshore Wind Laboratory (No. YJOWP-OF-2022A10),
608 the National Science Fund for Distinguished Young Scholars (No. 52025082) are
609 greatly appreciated.

610

611

612

613

614

615

616 **References:**

- 617 Amirafshari, P., Brennan, F. and Kolios, A. (2021). A fracture mechanics framework
618 for optimising design and inspection of offshore wind turbine support structures
619 against fatigue failure. *Wind Energy Sci.*, 6(3), 677–699.
620 <https://doi.org/10.5194/wes-6-677-2021>
- 621 Aydin, E., Öztürk, B., Kebeli, Y. E. and Gültepe, G. (2023). An Experimental Study on
622 the Effects of Different Pendulum Damper Designs on Structural Behavior. In
623 G. P. Cimellaro (Ed.), *Seismic Isolation, Energy Dissipation and Active Vibration
624 Control of Structures* (Vol. 309, pp. 240–253). Cham: Springer Interna-
625 tional Publishing. https://doi.org/10.1007/978-3-031-21187-4_18
- 626 Bergua, R., Robertson, A., Jonkman, J. and Platt, A. (2021). Specification Document
627 for OC6 Phase II: Verification of an Advanced Soil-Structure Interaction Model
628 for Offshore Wind Turbines (NREL/TP--5000-79938; p. NREL/TP--5000-
629 79938).
- 630 Bergua, R., Robertson, A., Jonkman, J., Platt, A., Page, A., Qvist, J., Amet, E., Cai, Z.,
631 Han, H., Beardsell, A., et al. (2022). OC6 Phase II: Integration and verification
632 of a new soil–structure interaction model for offshore wind design. *Wind En-
633 ergy*, 25, 793–810.
- 634 Branlard, E. (2017). *Wind Turbine Aerodynamics and Vorticity-Based Methods: Fun-
635 damentals and Recent Applications* (Vol. 7). Cham: Springer International Pub-
636 lishing.
- 637 Capaldo, M. and Mella, P. (2023). Damping analysis of floating offshore wind turbines
638 (FOWTs): a new control strategy reducing the platform vibrations. *Wind En-
639 ergy Sci.*, 8(8), 1319–1339. <https://doi.org/10.5194/wes-8-1319-2023>
- 640 Chen, C. and Duffour, P. (2018). Modelling damping sources in monopile-supported
641 offshore wind turbines. *Wind Energy*, 21(11), 1121–1140.
642 <https://doi.org/10.1002/we.2218>
- 643 Chen, C., Duffour, P., Dai, K., Wang, Y. and Fromme, P. (2021). Identification of aer-
644 odynamic damping matrix for operating wind turbines. *Mech. Syst. Signal Pro-
645 cess.*, 154, 107568. <https://doi.org/10.1016/j.ymssp.2020.107568>
- 646 Chen, C., Duffour, P. and Fromme, P. (2020). Modelling wind turbine tower-rotor in-
647 teraction through an aerodynamic damping matrix. *J. Sound Vib.*, 489, 115667.
648 <https://doi.org/10.1016/j.jsv.2020.115667>
- 649 Chen, C., Duffour, P., Fromme, P. and Hua, X. (2021). Numerically efficient fatigue
650 life prediction of offshore wind turbines using aerodynamic decoupling. *Renew.
651 Energy*, 178, 1421–1434. <https://doi.org/10.1016/j.renene.2021.06.115>
- 652 Colwell, S. and Basu, B. (2009). Tuned liquid column dampers in offshore wind tur-
653 bines for structural control. *Eng. Struct.*, 31(2), 358–368.
654 <https://doi.org/10.1016/j.engstruct.2008.09.001>
- 655 Dai, K., Huang, H., Lu, Y., Meng, J., Mao, Z. and Camara, A. (2021). Effects of soil–
656 structure interaction on the design of tuned mass damper to control the seismic
657 response of wind turbine towers with gravity base. *Wind Energy*, 24(4), 323–
658 344. <https://doi.org/10.1002/we.2576>

- 659 Dai, S., Han, B., Wang, B., Luo, J. and He, B. (2021). Influence of soil scour on lateral
660 behavior of large-diameter offshore wind-turbine monopile and corresponding
661 scour monitoring method. *Ocean Eng.*, 239, 109809.
662 <https://doi.org/10.1016/j.oceaneng.2021.109809>
- 663 Den Hartog, J. P. (1957). *Mechanical Vibrations*. Fourth Edition. *Aeronaut. J.*, 61(554),
664 139–139.
- 665 Dinh, V.-N. and Basu, B. (2015). Passive control of floating offshore wind turbine nacelle
666 and spar vibrations by multiple tuned mass dampers. *Struct. Control Health*
667 *Monit.*, 22(1), 152–176. <https://doi.org/10.1002/stc.1666>
- 668 DNVGL-RP-0005. (2014a). RP-C203: Fatigue design of offshore steel structures.
- 669 DNV-OS-J101. (2014b). Design of Offshore Wind Turbine Structures.
- 670 Fard, M. M., Erken, A., Erkmen, B. and Ansal, A. (2022). Analysis of Offshore Wind
671 Turbine by considering Soil-Pile-Structure Interaction: Effects of Foundation
672 and Sea-Wave Properties. *J. Earthq. Eng.*, 26(14), 7222–7244.
673 <https://doi.org/10.1080/13632469.2021.1961936>
- 674 IEC 61400-3-1. (2019). Wind energy generation systems Part 3-1: Design requirements
675 for fixed offshore wind turbines.
- 676 Jonkman, B. J. and Buhl, M. L. (2006). *TurbSim User's Guide*. Tech. Rep., 500, 39797.
- 677 Jonkman, J., Butterfield, S., Musial, W. and Scott, G. (2009). Definition of a 5-MW
678 Reference Wind Turbine for Offshore System Development (NREL/TP-500-
679 38060, 947422; p. NREL/TP-500-38060, 947422).
- 680 Jung, S., Kim, S.-R., Patil, A. and Hung, L. C. (2015). Effect of monopile foundation
681 modeling on the structural response of a 5-MW offshore wind turbine tower.
682 *Ocean Eng.*, 109, 479–488.
- 683 Klaus, H., Dirk, J. O. and Peter, M. (1973). Measurements of wind-wave growth and
684 swell decay during the joint North Sea wave project (JONSWAP).
- 685 Lackner, M. A. and Rotea, M. A. (2011a). Passive structural control of offshore wind
686 turbines. *Wind Energy*, 14(3), 373–388. <https://doi.org/10.1002/we.426>
- 687 Lackner, M. A. and Rotea, M. A. (2011b). Structural control of floating wind turbines.
688 *Mechatronics*, 21(4), 704–719. <https://doi.org/10.1016/j.mechatronics.2010.11.007>
- 690 Liang, F., Chen, H. and Jia, Y. (2018). Quasi-static p-y hysteresis loop for cyclic lateral
691 response of pile foundations in offshore platforms. *Ocean Eng.*, 148, 62–74.
692 <https://doi.org/10.1016/j.oceaneng.2017.11.024>
- 693 Lu, D., Wang, W. and Li, X. (2023). Experimental study of structural vibration control
694 of 10-MW jacket offshore wind turbines using tuned mass damper under wind
695 and wave loads. *Ocean Eng.*, 288, 116015.
696 <https://doi.org/10.1016/j.oceaneng.2023.116015>
- 697 Ma, H. and Chen, C. (2021). Scour protection assessment of monopile foundation de-
698 sign for offshore wind turbines. *Ocean Eng.*, 231, 109083.
699 <https://doi.org/10.1016/j.oceaneng.2021.109083>

- 700 Mayall, R. O., McAdam, R. A., Byrne, B. W., Burd, H. J., Sheil, B. B., Cassie, P. and
701 Whitehouse, R. J. S. (2018). Experimental modelling of the effects of scour on
702 offshore wind turbine monopile foundations. In A. McNamara, S. Divall, R.
703 Goodey, N. Taylor, S. Stallebrass, and J. Panchal (Eds.), *PHYSICAL MODEL-
704 LING IN GEOTECHNICS, VOL 1* (pp. 725–730). Int Soc Soil Mech & Ge-
705 otechn Engr, Tech Comm 104 Phys Modelling Geotechn; Active Dynam;
706 Tekscan.
- 707 Nakagawa, H. and Suzuki, K. (1976). Local Scour Around Bridge Pier in Tidal Current.
708 *Coast. Eng. Jpn.*, 19(1), 89–100.
709 <https://doi.org/10.1080/05785634.1976.11924219>
- 710 Pedersen, D. M. and Askheim, H. (2021). Implementation of seismic soil-structure in-
711 teraction in OpenFAST and application to a 10MW offshore wind turbine on
712 jacket structure. Norwegian University.
- 713 Pelayo, F., Skafte, A., Aenlle, M. L. and Brincker, R. (2015). Modal Analysis Based
714 Stress Estimation for Structural Elements Subjected to Operational Dynamic
715 Loadings. *Exp. Mech.*, 55(9), 1791–1802. <https://doi.org/10.1007/s11340-015-0073-6>
716
- 717 Rezaei, R. (2017). Fatigue Sensitivity of Monopile-supported Offshore Wind Turbines.
718 University College London.
- 719 Rezaei, R., Duffour, P. and Fromme, P. (2018). Scour influence on the fatigue life of
720 operational monopile-supported offshore wind turbines. *Wind Energy*, 21(9),
721 683–696. <https://doi.org/10.1002/we.2187>
- 722 Rudolph, D., Bos, K. J., Luijendijk, A. P. and Rietema, K. (2016). Scour around off-
723 shore structures-analysis of field measurements.
- 724 Shahmohammadi, A. and Shabakhty, N. (2020). Pile Apparent Fixity Length Estima-
725 tion for the Jacket-type Offshore Wind Turbines under Lateral Loads Applica-
726 ble to Fatigue Analysis. *Int. J. Coast. Offshore Eng.*, 3(4), 25–33.
727 <https://doi.org/10.29252/ijcoe.3.4.25>
- 728 Shirzadeh, R., Devriendt, C., Bidakhvidi, M. A. and Guillaume, P. (2013). Experi-
729 mental and computational damping estimation of an offshore wind turbine on a
730 monopile foundation. *J. Wind Eng. Ind. Aerodyn.*, 120, 96–106.
731 <https://doi.org/10.1016/j.jweia.2013.07.004>
- 732 Song, J. and Achmus, M. (2023). Cyclic overlay model of p – y curves for laterally
733 loaded monopiles in cohesionless soil. *Wind Energy Sci.*, 8(3), 327–339.
734 <https://doi.org/10.5194/wes-8-327-2023>
- 735 Sørensen, P. H. S. and Ibsen, L. B. (2013). Assessment of foundation design for off-
736 shore monopiles unprotected against scour. *Ocean Eng.*, 63, 17–25.
- 737 Stieng, L. E. S. and Muskulus, M. (2020). Reliability-based design optimization of off-
738 shore wind turbine support structures using analytical sensitivities and factor-
739 ized uncertainty modeling. *Wind Energy Sci.*, 5(1), 171–198.
740 <https://doi.org/10.5194/wes-5-171-2020>
- 741 Tang, Z., Melville, B., Shamseldin, A., Guan, D., Singhal, N. and Yao, Z. (2023). Ex-
742 perimental study of collar protection for local scour reduction around offshore
743 wind turbine monopile foundations. *Coast. Eng.*, 183, 104324.
744 <https://doi.org/10.1016/j.coastaleng.2023.104324>

- 745 van der Tempel, J. (2006). Design of support structures for offshore wind turbines.
746 Technische Universiteit Delft.
- 747 Velarde, J., Kramhøft, C., Sørensen, J. D. and Zorzi, G. (2020). Fatigue reliability of
748 large monopiles for offshore wind turbines. *Int. J. Fatigue*, 134, 105487.
749 <https://doi.org/10.1016/j.ijfatigue.2020.105487>
- 750 Wang, G., Xu, S., Zhang, Q. and Zhang, J. (2023). An experimental study of the local
751 scour protection methods around the monopile foundation of offshore wind tur-
752 bines. *Ocean Eng.*, 273, 113957.
753 <https://doi.org/10.1016/j.oceaneng.2023.113957>
- 754 Wang, L., Zhou, W., Guo, Z. and Rui, S. (2020). Frequency change and accumulated
755 inclination of offshore wind turbine jacket structure with piles in sand under
756 cyclic loadings. *Ocean Eng.*, 217, 108045.
757 <https://doi.org/10.1016/j.oceaneng.2020.108045>
- 758 Wang, X., Zeng, X., Li, X. and Li, J. (2019). Investigation on offshore wind turbine
759 with an innovative hybrid monopile foundation: An experimental based study.
760 *Renew. Energy*, 132, 129–141. <https://doi.org/10.1016/j.renene.2018.07.127>
- 761 Zdravković, L., Taborda, D., Potts, D., Jardine, R., Sideri, M., Schroeder, F., Byrne, B.,
762 McAdam, R., Burd, H., Houlsby, G., et al. (2015). Numerical modelling of large
763 diameter piles under lateral loading for offshore wind applications. *Front. Off-
764 shore Geotech. III*, 759–764.
- 765 Zhang, F., Chen, X., Feng, T., Wang, Y., Liu, X. and Liu, X. (2022). Experimental
766 study of grouting protection against local scouring of monopile foundations for
767 offshore wind turbines. *Ocean Eng.*, 258, 111798.
768 <https://doi.org/10.1016/j.oceaneng.2022.111798>
- 769 Zhang, F., Chen, X., Yan, J. and Gao, X. (2023). Countermeasures for local scour
770 around offshore wind turbine monopile foundations: A review. *Appl. Ocean
771 Res.*, 141, 103764. <https://doi.org/10.1016/j.apor.2023.103764>
- 772 Zhang, H., Liang, F. and Zheng, H. (2021). Dynamic impedance of monopiles for off-
773 shore wind turbines considering scour-hole dimensions. *Appl. Ocean Res.*, 107,
774 102493. <https://doi.org/10.1016/j.apor.2020.102493>
- 775 Zhang, R., Zhao, Z. and Dai, K. (2019). Seismic response mitigation of a wind turbine
776 tower using a tuned parallel inerter mass system. *Eng. Struct.*, 180, 29–39.
777 <https://doi.org/10.1016/j.engstruct.2018.11.020>
- 778
- 779
- 780
- 781